ISSN 1063-7397, Russian Microelectronics, 2025, Vol. 54, No. 5, pp. 494–505. © Pleiades Publishing, Ltd., 2025.

Complementary Studies of Aluminum Thin Films: Resistivity and Real Structure

A. A. Lomov[a], *, M. A. Tarasov[b], **, K. D. Shcherbachev[c], *, A. A. Tatarintsev[a], ****, and A. M. Chekushkin[b], *******

[a] *National Research Center "Kurchatov Institute," Moscow, Russia*

[b] *Kotelnikov Institute of Radio Engineering and Electronics, Russian Academy of Sciences, Moscow, Russia*

[c] *National University of Science and Technology (MISiS), Moscow, Russia*

**e-mail: andlomov@ftian.ru*

***e-mail: tarasov@hitech.cplire.ru*

****e-mail: chterb@gmail.com*

*****e-mail: tatarintsev@ftian.ru*

******e-mail: chekushkin@hitech.cplire.ru*

Received June 4, 2025; revised July 15, 2025; accepted July 20, 2025

Abstract—The results of complex studies of the temperature dependence of the electrical resistance of thin magnetron Al films on their structural characteristics—morphology, surface roughness, microstructure, and density—are presented. In order to establish a fundamental connection between the specific resistance and the structural features of the films, they are deposited on standard Si(111) substrates in a two-stage growth mode with the formation of homobuffer layers (HBL) in the temperature range from 293 to 800 K. Structural characterization of the samples is performed using scanning force and electron microscopy, X-ray diffractometry, and reflectometry. It is shown that the magnitude and temperature dependence of the specific resistance of aluminum films can be changed by varying the growth conditions of the HBL, which allows deposition of films with different density profiles across the thickness. It is found that a magnetron 120-nm aluminum film on a 700 K HBL with a constant density of 2.66 g/cm^3 has a specific resistance of $\rho_{RT} = 2.69$ μOhm cm and $T_c = 1.22$ K. Al films with variable density have a residual resistance of ~30 μOhm cm. The main contribution to the resistance of such films is made by intergranular regions with lower density, which is reliably recorded by the X-ray reflectometry method.

Keywords: thin films, aluminum, density profile, microstructure, resistivity, superconducting transition temperature, X-ray diffractometry and reflectometry, SEM and AFM microscopy

DOI: 10.1134/S1063739725600554

1. INTRODUCTION

In recent years, there has been renewed interest in the study of thin aluminum films due to a wide range of possible applications ranging from traditional anticorrosion and reflective coatings, as well as micro-, opto-, and power electronics [1], to X-ray mirrors [2], elements of plasmonics, and quantum computers [3, 4]. Interest in nanoscale aluminum films is driven by the task of creating compact superconducting SIS devices based on tunnel junctions, ultrahigh-sensitivity magnetic field sensors or superconducting quantum interference devices (SQUIDs) [5], as well as microwave frequency range devices based on the kinetic inductance of a superconducting film [6]. In the first case, smooth, uniform films with minimal residual resistance are required. In the second case, smooth films are also required, but with high specific resistance to obtain maximum kinetic inductance. The requirement to increase the critical temperature of the transition of Al films to the superconducting state when developing growth methods is a priority for all tasks. Such conflicting requirements in each case can be met by the correct choice of the method and conditions for film growth: the crystalline structure of the substrate, the temperature and growth rate, the composition and pressure of the gas, etc. Depending on the tasks, aluminum films are formed using traditional methods of vacuum thermal spraying and magnetron sputtering, as well as more technologically advanced ones: molecular beam epitaxy and atomic layer deposition [7–10].

The electrical resistance of a metal and its temperature dependence are determined by various mechanisms of the scattering of current carriers as they move along a conductor. The resistance value is directly related to the characteristics of its real structure: elemental composition, impurities, sizes and stresses of crystallites, microstructure, texture, structural defects,

pores, and amorphous inclusions. In bulk samples, the scattering of current carriers occurs due to electron-phonon interaction (on atoms at the nodes of the crystal lattice). In this model, the ohmic resistance shows a linear dependence in the temperature range close to room temperature. Such a dependence was observed during the first measurements of the resistance of noble metals [11]. This mechanism is the main one in the case of a perfect single crystal, or when the crystallite sizes d is much greater λ than the mean free path of the charge carriers. When $d \le \lambda$, additional scattering occurs at the crystallite boundaries, giving a constant contribution to the resistance of the sample, which is weakly dependent on temperature. The scattering of current carriers on structural defects of the crystal lattice does not depend on temperature and makes a constant contribution to the resistance of the material [12]. The last two types of carrier scattering are responsible for the residual resistance ρ_0. We do not consider here the resistance mechanism of the material near the critical temperature T_c of its transition into the superconducting state, which is associated with quantum mechanical phenomena. When analyzing the electrical resistance of a nanoscale film, it is necessary to additionally take into account the spatial distortions of its surfaces (the external and internal boundaries with the substrate), characterized by the morphology, roughness value, and lateral correlation length and deformation of the crystal lattice. In particular, the contribution to the film's resistance will be given by the scattering of current carriers not only at the grain boundaries but also at the roughness of both its boundaries [13] due to the commensurability of the film thickness t and the mean free path.

The analysis and consideration of all structural features of metal films on their resistance began and was discussed by Thomson [14] even before the discovery of the phenomenon of superconductivity in 1911 [15]. Thomson considered a transport geometric model of the motion of electrons reflected from two surfaces of a film of thickness t at a constant mean free path λ. The later model of Fuchs and Sondheimer (FS) [16, 17] took into account the statistical distribution λ and the morphology of the film surface. The modern model of Mayadas and Shatzkes (MS) [18, 19] adds grain boundary transparency and average grain size. The influence of the internal size effect, caused by the polycrystalline structure of metal films, on the coefficients of reflection, as well as transmission and absorption of electromagnetic waves, was studied in [20]. The work by Zhang et al. [21] presents measurements of the resistance as a function of the thickness of Al, Cu, Ag, and CuAu I films and analyzes them based on the FS, MS, and electron mean free path models. The authors consider the critical thickness t_c of the films, below which a pronounced increase in resistance is observed, as evidence of the manifestation of the size effect. To minimize the size effect, materials with a shorter electron mean free path should be selected. This observation echoes the conclusions of the phenomenological model of Andrews [22], according to which the resistivity is inversely proportional to the average grain diameter. A disadvantage of the Andrews model is the lack of consideration of the actual particle size distribution, which may be the cause of the temperature dependence of the proportionality parameter (A).

Attempts by the authors [22–25] to conduct studies of the dependence of film resistance on a specific scattering mechanism failed due to the integral nature of the phenomenon and the need to take into account a large number of parameters determined by the methods and conditions of growth. This complicates the unambiguous interpretation of the studies carried out on the transport properties of films. The structural characterization of films is usually performed by X-ray diffractometry (XRD, GIXRD), atomic force microscopy (AFM), and scanning electron microscopy (SEM) and, less commonly, by scanning transmission microscopy (STEM). In most cases, the obtained results are difficult to compare with the data of electrophysical measurements, since AFM and SEM are local methods, and XRD and GIXRD provide information on the phase composition and microstructure of the film volume, and not on its boundaries and structural defects. At the same time, it is noted that not only the morphology and roughness of the boundaries but also the density of the films strongly depends on the growth technology. The density distribution across the film thickness can be reconstructed using X-ray reflectometry (XRR) [26]. Analysis of the intensity of the specular and diffuse components of total scattering in XRR allows us to judge the structural features of the film. The use of X-ray reflectometry for the analysis of thin metal films began as early as 1931 by H. Kiessig [27]. However, nowadays it is most often used to study surfaces, multilayer mirrors, and semiconductor structures [28]. The sensitivity of the XRR method to the inner boundary of a 150 nm aluminum film was demonstrated in [29] in a study of the influence of a homobuffer layer (HBL) on a silicon substrate on the structural and mechanical properties of the film.

In this paper, we show the relationship between the specific resistance of thin magnetron films of aluminum and their real structure (morphology, microstructure, surface roughness, density profile, composition). In order to trace the influence of the transformation of the film structure on the temperature dependence of resistance, they were deposited on a silicon substrate in a two-stage growth mode at a temperature ranging from 293 to 800 K.

2. EXPERIMENTAL

Aluminum films were deposited using a magnetron sputtering setup (Kurt J. Lesker Company Ltd., Germany) in DC argon plasma discharge mode, at a power of 500 W, with an Al (99.995%) target. Standard Si(111) wafers with a 4-degree misorientation were used as substrates. Before the deposition of aluminum films, the Si(111) substrates were cleaned in an ultra-

sonic bath in an acetone environment. The remaining contaminants were washed off with distilled water. The substrates were then sent to the growth chamber of the magnetron. Al films were deposited on the substrate in a two-stage mode. The first stage of the film deposition process consisted of forming an aluminum layer (HBL) on the surface of the Si(111) substrate at a rate of 0.13 nm/s and a calculated thickness of ~15 nm at temperatures from 293 to 800°K with an interval of 100 K. After cooling the substrate with the HBL layer to room temperature (*RT*), in the second stage, additional deposition of aluminum occurred at a rate of 1.7 nm/s and a temperature of 19–21°C before the formation of a 150 nm film.

The temperature dependence of resistance $R(T)$ and critical temperature T_c of the transition to the superconducting state was measured using the 4-probe method in a HELIOX-AC-V (Oxford Instruments) closed-cycle cryostat of the sorption type on Helium-3 in the range of 280 mK to 300 K.

Scanning electron microscopy was used to measure the local thickness of the films, as well as analyze their thickness homogeneity and surface morphology. The oxygen impurity in the films was estimated based on the X-ray spectral data. The experiments were performed on a Carl Zeiss Ultra 55 scanning electron microscope equipped with an Oxford Instrument INCA X-act energy-dispersive X-ray spectrometer (EDS).

For the statistical description of the surface morphology of the films—the roughness values and correlation coefficient of surface inhomogeneities—the AFM method was applied using a Dimension Icon microscope (Bruker) and commercial RTESPA-300 cantilevers. The cantilever tip was made of silicon with a nominal radius of 8 nm, a resonance frequency of 300 kHz, and a precalibrated (Bruker) nominal stiffness of 40 N/m. The scanning frequency was 1 Hz with the given peak force value of ~3 nN and a forward linear scanning direction.

X-ray structural measurements were taken on a SmartLab diffractometer (9 kW, CBO optics, CuK_α radiation) in parallel-beam geometry. The microstructure (phase composition, texture, crystal lattice parameter a, and crystallite size d) of the Al films was studied based on XRD diffraction patterns ($2\theta/\omega$) and GIXRD (2θ, $\omega = 0.5°$, off-plane geometry), measured with a Soller slit of 0.114° installed in front of the detector window. The XRR curves ($2\theta/\omega$) were measured in the angular range of 0° to 4° using a Ge(220) slit monochromator with double reflection and an X-ray beam 50-μm wide. To reconstruct the depth density distribution profile $D(z)$ from the XRR data, a technique based on the differential evolution algorithm was used [30].

3. RESULTS

3.1. Film Resistance

The temperature dependencies of specific resistance $\rho(T)$ of the studied aluminum films of Al/Si(111) samples (TA1, TA5) depending on the deposition temperature of the HBL at 300 and 700 K, respectively, are presented in Fig. 1. For comparison, similar curves for MBE Al films are added to the figure: 60 nm, 200 nm [31] on an Si(111) silicon substrate and 60 nm [32] on an $Al_2O_3(0001)$ sapphire. As a reference, the temperature dependence of the specific resistance $\rho(T)$ for 99.998% metallurgical bulk aluminum (MA) [33] is also given.

It is evident that the resistance of TA1 and TA5 films with HBLs deposited at 300 and 700 K differs both in magnitude and in the functional form of its decrease with decreasing temperature. For example, the TA5 film at room temperature has a specific resistance value of $\rho_0 = 2.69$ μOhm cm close to the value of 2.62 · for the bulk material [33, 34]. The film resistance of the TA1 sample is almost an order of magnitude greater than this value. Near temperature T_c of the transition to a superconducting state, the ratio of their resistance values reaches 40. At the same time, temperatures T_c for TA5 and TA1 films are 1.22 and 1.33 K, respectively, which significantly exceed the critical temperature for bulk aluminum $T_c = 1.18$ K [34]. Similar differences can be observed for the resistance of the other samples presented. To explain these features of the resistance of films, it is necessary to know the characteristics of their real structure.

3.2. Film Morphology

Figures 2a–2f show AFM images of scans of the surface of the grown Al/Si(111) films with a thickness of ~150 nm (Table 1) with randomly located individual and fused (combined) crystallites observed on them with characteristic dimensions of 50–300 nm. It should be noted that the contrast of images (a), (b), and (c) is slightly higher compared to images (d), (e), and (f) from the films deposited on HBLs at 600, 700, and 800 K, respectively. When comparing images (a–f), the features in the morphology of the film surfaces are clearly visible: (*1*) presence of modes in the distribution of crystallites by size; and (*2*) difference in the homogeneity of the contrast: color intensity over the scan area. Visually, we can distinguish the image in Fig. 2e, which contains the surfaces of large (300 nm) crystallite grains and small (50 nm) ones between them. According to the EDS spectra, the main chemically active impurity in the films is oxygen, which is present in a ratio of 1 : 7 relative to aluminum.

The numerical processing of SEM images of film surfaces to determine the values of *rms* roughness, correlation length ξ, and the Hurst exponent h was performed using software. For evaluation of the *rms*, the Gwyddion-2.60 program [35] was used. The quantitative analysis of ξ and h was performed using the autocorrelation function $C(r_1, r_2)$ (1) for topographic data (WSxMv5.0 Develop 10.2) [13, 36, 37]:

$$C(r_1, r_2) = \sum_{x,y} D(x, y)D(x + r_1, y + r_2). \quad (1)$$

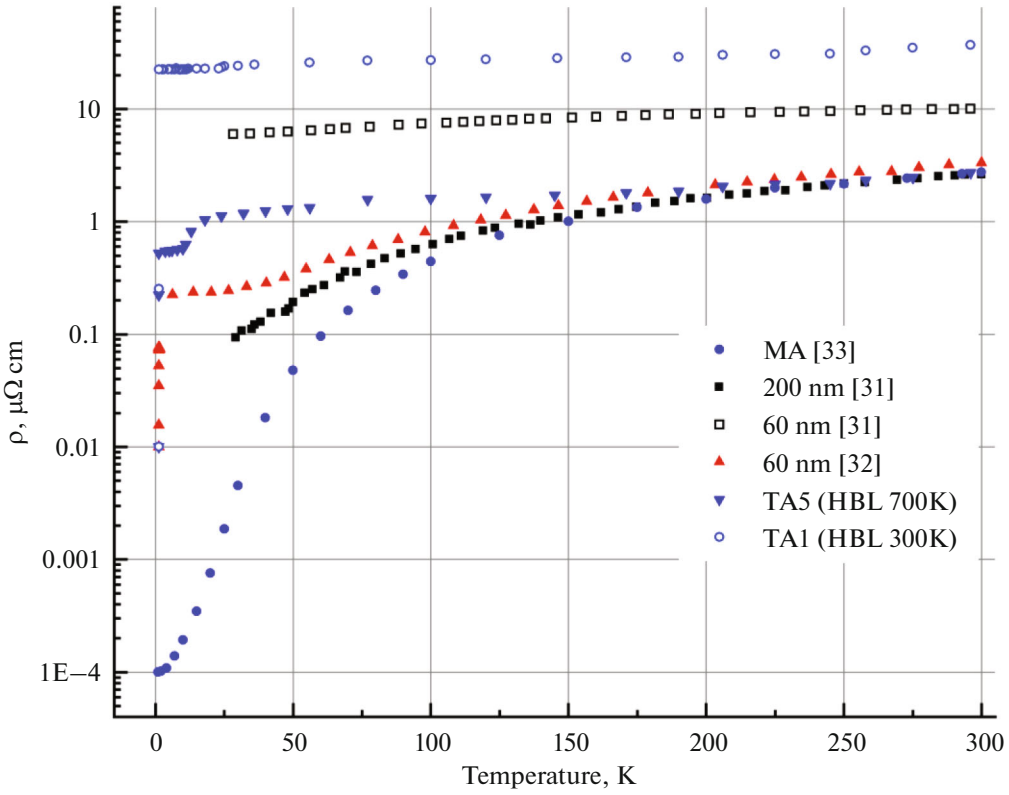

Fig. 1. Temperature dependencies of the specific resistance of aluminum in the form of thin films obtained by magnetron sputtering (TA1, TA5), by molecular beam epitaxy (60 nm, 200 nm [31]; 60 nm [32]), and metallurgical material [33].

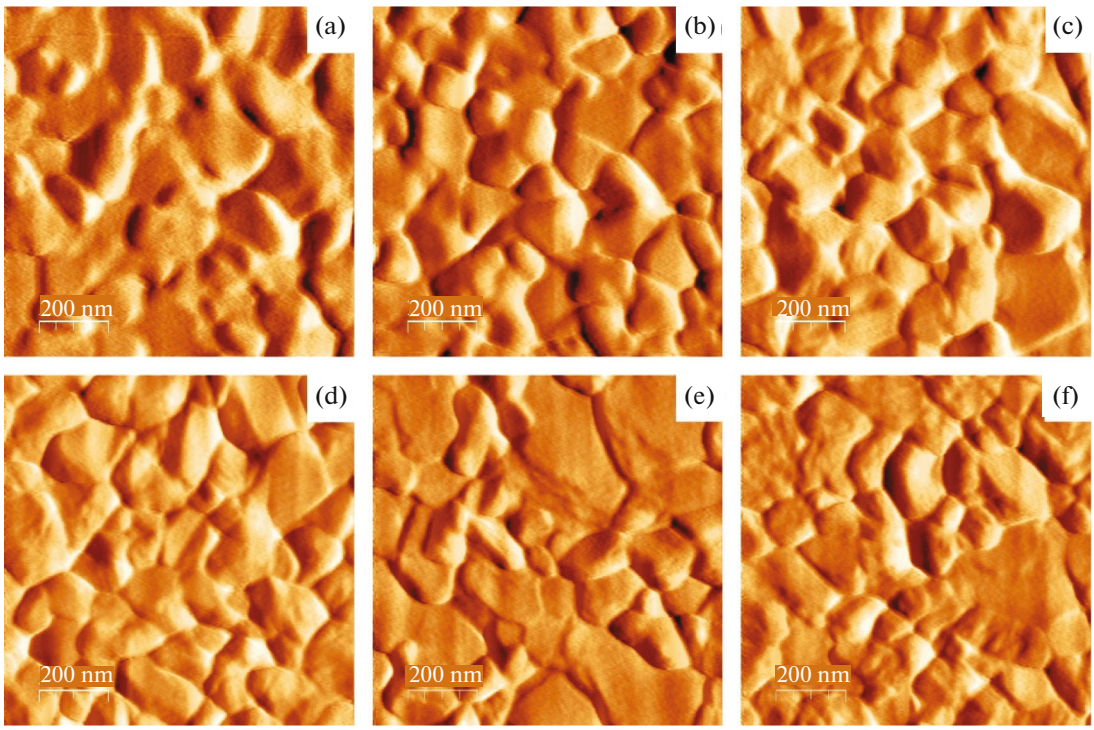

Fig. 2. AFM images of the surface of two-stage magnetron films of Al (TA1–6) on Si(111) with HBL layers deposited at (a) 300 K, (b) 400 K, (c) 500 K, (d) 600 K, (e) 700 K, (f) 800 K.

Table 1. Morphological parameters of the surface of magnetron Al films depending on the growth temperature of the HBL

Sample Al/Si(111)	HBL layer growth temperature, K	Film thickness, d, nm SEM	Roughness *rms*, nm AFM	Correlation length ξ, nm AFM	The Hurst parameter h AFM
TA1	300	140(3)	5.3	40.3(1)	0.853(4)
TA2	400	144(3)	6.1	35.9(2)	0.791(7)
TA3	500	139(3)	6.8	39.8(2)	0.783(7)
TA4	600	150(3)	5.9	34.7(2)	0.82(1)
TA5	700	155(2)	5.4	30.6(2)	0.86(1)
TA6	800	143(3)	5.3	33.4(4)	0.84(1)
Si(111)-sub	–	–	0.3	–	–
HBF [29]	700	150(1)	6.5	57.6(4)	0.990(6)

On the plane (x, y), the view $C(r_1, r_2)$ appears as a maximum at the origin with smoothly falling "tails." In the absence of anisotropy in the plane of the film, the autocorrelation function in polar coordinates can be written as

$$C(r) \sim \exp\left[\left(-\frac{r}{\xi}\right)^{2h}\right], \quad (2)$$

where r is the distance from the maximum of the correlation function. Here parameter ξ is the short-range correlation length at which the characteristic parameters (e.g., roughness, color, etc.) of the studied object do not change within the limits of statistical uncertainty (become statistically independent). The Hurst exponential exponent h $(0 < h < 1)$ characterizes the fractal nature of the surface. The h value determines not only how uniform the image of an object is but also the blurriness (sharpness) of its boundaries. At $h \le 0.5$, the analyzed parameter of the studied surface area is a random variable and its surface is nonuniform. In contrast, at $h > 0.5$ the surface becomes more homogeneous. The results of the statistical analysis of the images in Fig. 2 are presented in Table 1.

3.3. XRD and GIXRD Diffractometry

The microstructural features of the aluminum film samples are revealed in the X-ray diffraction patterns presented in Fig. 3 for symmetric XRD (a) and sliding GIXRD (b) measurement geometry.

The angular positions of the diffraction maxima correspond to the fcc phase of metallic aluminum with constant a = 0.405 nm (PDXL #01-080-5308). In general, the appearance of the diffraction patterns corresponds to those previously published [29] and reflects the patterns of the microstructure of metal films depending on the conditions of magnetron sputtering. It can be seen that the film of sample TA1 with a 300 K HBL layer grew as expected, strongly textured in the [111] direction. This is clearly seen when comparing the ratio of the most intense diffraction peaks for reflections 111 and 200 (Fig. 3a). The remaining low intensity reflections 220 and 222 are not shown. For the remaining samples TA2–TA6, no pronounced texture is observed due to further film growth on the distorted surface of the HBL layer [38].

The GIXRD diffraction patterns (Fig. 3b) are recorded from crystalline planes deflected at different angles from the film surface. Due to the polycrystalline nature of the films and the wide angular dispersion of the crystallite faces, the number of intense reflections entering the detector is greater. In Fig. 3b it is evident that the intensity ratios of the corresponding reflections on the GIXRD diffraction patterns change insignificantly, with the exception of reflections from the film of sample TA5 with a 700 K HBL. A sharp increase in the intensity of 220 reflection is observed for it. In the kinematic approximation, the intensity of reflection from a polycrystalline film is determined by the number of crystalline planes for which the Bragg conditions are simultaneously satisfied. The intense 220 reflection of sample TA5 indicates significant ordering of the (110) planes, either due to crystallite intergrowth or the formation of large crystallites. This result should be evident when analyzing the X-ray reflectometry curves. The XRR method allows us not only to estimate the average film density but also to reconstruct the film density profile by thickness [26, 28, 40].

3.4. XRR Reflectometry

The experimental and calculated reflectometry curves from samples of Al/Si(111) films with HBLs deposited at 300, 600, and 700 K are shown in Fig. 4. The main parameters of the XRR curves—angle of total external reflection $\theta_c \sim \sqrt{D}$ (D is the film density) and period $\Delta 2\theta \approx \lambda Cu/t$ of the fundamental oscillations (Kiessig fringes), where λCu is the wavelength of the characteristic radiation of copper—confirm the formation of aluminum films with a thickness ~150 nm. However, there are characteristic differences between the curves. First of all, we note the difference in

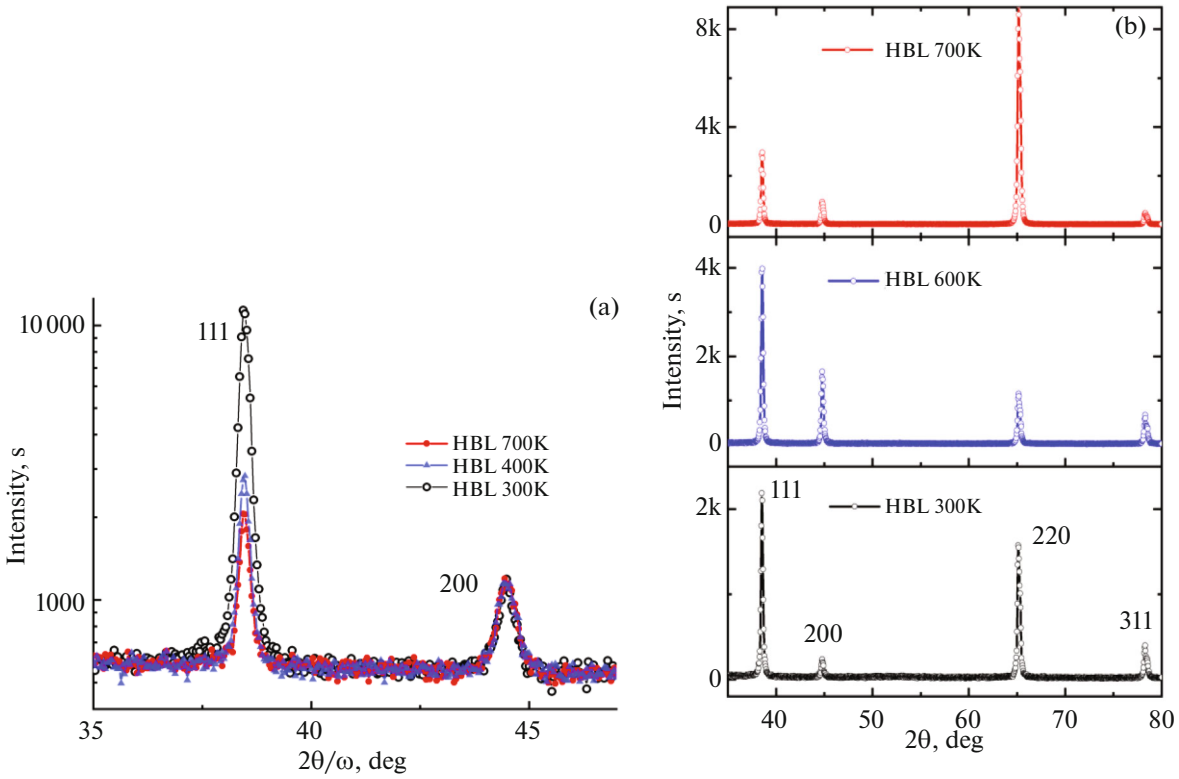

Fig. 3. Diffraction patterns of the studied Al/Si(111) films with HBL layers deposited at different temperatures: (a) XRD symmetrical scanning and (b) GIXRD off-plane scanning at an angle of incidence of the X-ray beam φ = 0.5°. CuK_α radiation.

reflection intensity as angle 2θ increases, the presence of a weak long-period oscillation (elevation at angles in the range of 1°–1.5°), as well as the number and amplitude of the observed oscillations. Additional studies using the reciprocal space section method showed that the specular scattering component makes the main contribution to the reflection intensity in the tails of the XRR curves. Therefore, the difference between the XRR curves observed in Fig. 4 is associated with the features of their structure near the surface and the density distribution across the thickness of the Al layer. The density distribution profile (Fig. 5) across the thickness of the sample films was reconstructed by fitting the calculated curves to the experimental XRR in the range of $0.3° < 2\theta < 4°$ (the range from 2 to 4 degrees is not shown in Fig. 4).

Methods for reconstructing the density profile of a film or surface layer from reflectometric data are based on a trial-and-error method, in which the model parameters of the sample are changed until the best match between the experimental and calculated XRR curves is achieved. The specular component of the reflection curve was calculated using the Parratt equations [26], and the intensity of diffuse scattering measured with sufficient statistics was considered as the background. The mathematical procedure for fitting the calculated curves to the experimental ones was carried out based on the differential evolution algorithm, taking into account the features of the X-ray diffraction data [30]. This algorithm belongs to the class of global optimization methods. It should be noted that the maximum accuracy of density value recovery is due to the phenomenon of total external reflection, depends on the quality of the sample and experimental data, and does not exceed 2%.

The coefficient of reflection of X-ray radiation from a film with surface distortions was calculated by representing the rough boundary in the form of a series of smooth transition layers with a refractive index [39, 40],

$$n_j(z) = \frac{n_j + n_{j+1}}{2} + \frac{n_j + n_{j-1}}{2} Erf\left(\frac{z}{\sqrt{2}\sigma_j}\right), \qquad (3)$$

where a n_j and n_{j+1} are the refractive indices for two media far from the interface, z is the depth, σ is the width of the distribution of *Erf* function. The process was repeated until it was possible to reduce the value of the objective function describing the matching criterion. The χ^2 criterion [41] was chosen as the criterion for the coincidence of the calculated curve to the experimental one,

$$\chi^2(\boldsymbol{\beta}) = \frac{1}{n - n_p} \sum_{i=1}^{n} \frac{\left(I_i^E - I_i^T(\boldsymbol{\beta})\right)^2}{s_i^2}, \qquad (4)$$

where s_i is the intensity measurement error I_i^E at the ith point; n is the number of points on the curve; and

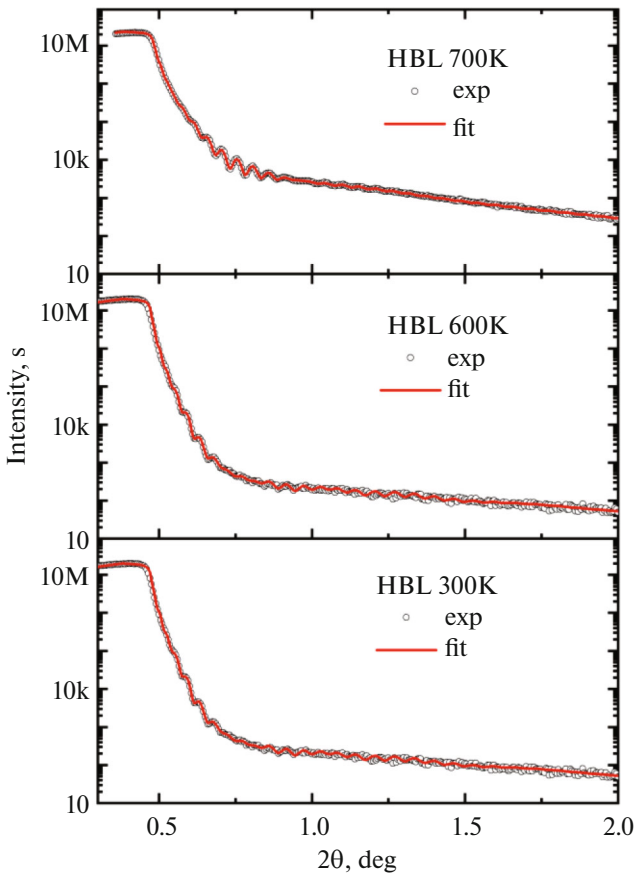

Fig. 4. Experimental background-free (light circles) and fitted (solid lines) X-ray reflectometry curves from the studied Al films ($t \sim 150$ nm) with HBLs on Si(111). CuK_{α_1} radiation. The magnitude of $\chi^2 \le 1.5$ was for all fitted curves.

n_p is the number of changeable parameters of the model (the dimension of the vector of optimization parameters **β**). The uncertainty in determining the vector of optimization parameters **β** can be estimated through the inverse covariance matrix C_{kl}^{-1} (of dimension $n_\text{p} \times n_\text{p}$), which is calculated using the Marquardt–Levenberg method [42],

$$C_{kl}^{-1} = \sum_{i=1}^{n} \frac{1}{s_i^2} \left[\frac{\partial I_i^T}{\partial \beta_k} \frac{\partial I_i^T}{\partial \beta_l} \right]_{\boldsymbol{\beta}=\boldsymbol{\beta}_0}, \quad (5)$$

$\boldsymbol{\beta}_0$ is the vector of parameters obtained after the completion of the optimization procedure. Then the standard error σ_i can be determined from the following relationship:

$$\sigma_i = \sqrt{C_{ii}\chi^2}, \quad (6)$$

where C_{ii} is the diagonal element of the covariance matrix.

4. RESULTS AND DISCUSSION

The temperature dependencies of the specific resistance $\rho(T)$ of the samples of aluminum films in Fig. 1 can be divided into two groups according to the value of their resistance at room temperature. In the first group, the resistance is close to that of metallurgical aluminum $R_{01} \approx R_{0b}$ (sample MA), and in the second group the resistance is significantly greater $R_{02} > R_{0b}$. The dependencies of the resistance $R(T)$ of film samples on their real structure in the developed Dobierzewska–Mozrzymas and Warkusz model [43]

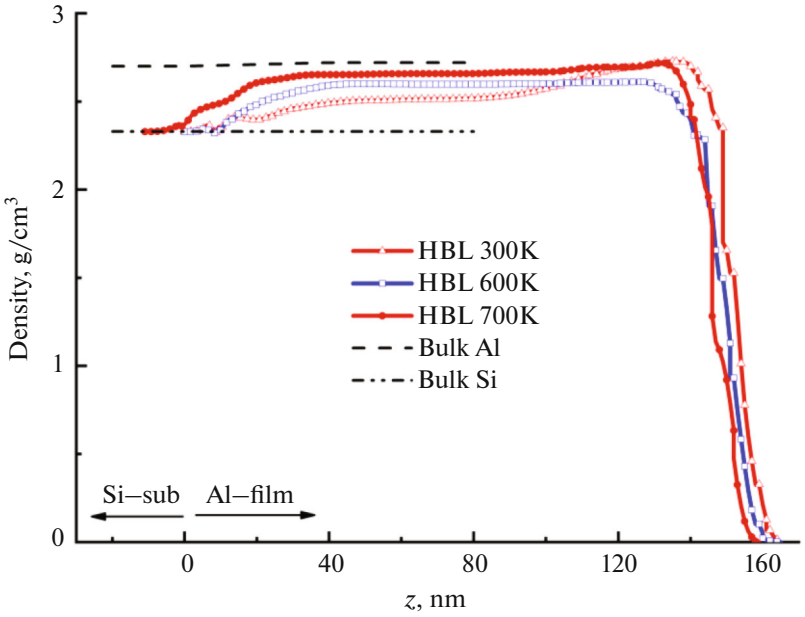

Fig. 5. Thickness density distribution of Al/Si(111) films with HBL layers based on X-ray reflectometry data. Dashed lines are densities of bulk materials [34].

based on the theories [16–19] are presented as a sum of the contributions

$$R(T) = R_b + R_d + R_t, \quad (7)$$

where R_b is the electron–phonon interaction, R_d is the contribution to the resistance from electron scattering at the grain boundaries of crystallites of size d: $R_d = 3\lambda RR_b/2d(1 - R)$, R is the reflection coefficient from the grain boundary, λ is the mean free path of electrons, and R_t is the additional resistance due to electron scattering at the outer boundaries of thin films at $\lambda \sim t$. $\rho_t = 3\lambda(1 - f)\rho_b/8t$ (f is the coefficient of specular reflection at the boundaries). The mean free path of electrons in aluminum is $\lambda = 16$ nm [44]. Assuming that λ depends weakly on temperature, and the thickness of the aluminum films under consideration is greater than λ, we will assume that the contribution to the resistance $R(T)$ is determined by the electron-phonon interaction in the form of the reference $R_b(T)$ and residual resistance R_0. It is clearly seen that the dependencies of $R_{01}(T)$ of the presented samples practically coincide with the course of $R_b(T)$ for the MA sample up to a temperatures above 150 K. This means that the contribution to resistance from internal grain boundaries and other structural defects is negligible. As the temperature decreases further, the main contribution becomes the residual resistance R_0, depending on the actual structure of the samples. In Fig. 1 it is evident that the temperature dependencies of resistance at low temperatures for the samples differ. This is primarily due to the tails of the grain size distributions of the crystallites, which vary depending on the growth method and film thickness. It should be noted that, in the metallurgical sample MA, all crystallites have dimensions $d \gg \lambda$, while in magnetron films their dimensions are distributed in the range from 20 to 300 nm (Fig. 2), (Fig. 1 [38]). Analysis of the half-widths of XRD reflections (Fig. 3) based on the Scherrer formula [45] allows us to confirm the presence in the sample of a significant number of crystallites with an average size of $d = 25$–50 nm, commensurate with the value of λ and contributing to R_0 at a low temperature. The 200 nm [31] and 60 nm [32] films obtained by the MBE method are more textured and mainly contain crystallites (1000 nm [31]) with an average lateral size of $d > \lambda$. Their dependencies $R_0(T)$ in Fig. 1 are located closer to $R_b(T)$ at $T <$ 100 K. However, these films also contain residual resistance due to the scattering of electrons at the internal and external boundaries of small grains due to possible voids between them.

Samples TA1 and 60 [32] are characterized by the dependencies of specific resistance $R_{02}(T)$, in which the predominant contribution to the resistance, in addition to scattering at internal grain boundaries, comes from scattering at structural defects of the films: external grain boundaries, amorphous inclusions, and pores. The magnitude of this scattering at $T = 300$ K significantly exceeds R_b, which is clearly visible in Fig. 1. The residual resistance of these samples depends weakly on temperature due to the smaller contribution of the electron-phonon interaction inside the crystallite grains to the total resistance. Indeed, the sections of the diffraction patterns shown in Fig. 3 are not fundamentally different, and the half-widths of the Bragg maxima reflections practically coincide with the values for the TA5 sample. This means that grain boundary scattering does not make a major contribution to the resistance. To ensure that the surface does not influence the observed pattern, let us turn to the AFM data.

The AFM images of 1×1 μm surface areas (Fig. 2) show the presence of randomly located crystallite grains of 50–300 nm in the aluminum films, depending on the deposition temperature of the HBL layer. In general, the images themselves differ little. This indicates that near the outer boundary of the film the morphological parameters of the films are close to each other. The surface images show qualitative differences in the sharpness of grain boundaries, their average size, and dispersion. It is clear that the largest average grain size with diffuse boundaries is observed (Fig. 2a) for sample TA1. However, the maximum grains with a size of 300 nm (Fig. 2e) with sharp boundaries belong to sample TA5. At the same time, a significant number of grains of 70 nm are observed on its surface. These observations allow us to correctly interpret the data in Table 1. It can be seen from it that for all samples the value of grain roughness is $rms = 5$–6 nm. This is an expected result, since films thicker than 120 nm are assumed to be continuous and were grown under the same conditions. However, the correlation length parameter and the Hurst parameter differ. The microstructure of 150-nm-thick films still "remembers" the surface relief of the HBL, which depends on its deposition temperature. The largest correlation length $\xi =$ 40 nm corresponds to sample TA1, which is consistent with the closely spaced large blocks (Fig. 2a). For sample TA5, the parameter $\xi = 30$ nm. This is surprising for a smooth surface (Fig. 2f), if we disregard the bimodal distribution of grain sizes observed in this figure. The resulting discrepancy is removed by comparing the values of the Hurst parameter $-h$ (Table 1). Despite their small difference between themselves (compare with [29]), parameter h adequately reflects the homogeneity of the film surface. The Hurst exponential exponent h ($0 < h < 1$) characterizes the fractal nature of the surface. The value of h determines not only how uniform the image of an object is but also the blurriness (sharpness) of its boundaries. It is considered that for small values of h, the characteristic parameter of the studied surface area is a random variable, and the surface itself is nonuniform. In contrast, when h tends to 1, the image of the surface of the area (grain) becomes more uniform, and the area has sharp boundaries. The maximum value for $h = 0.860$ corresponds to sample TA5 with a 700 K HBL. The value $h = 0.860 > h = 0.853$ for sample TA1, which confirms the maximum smoothness of the film surface of sam-

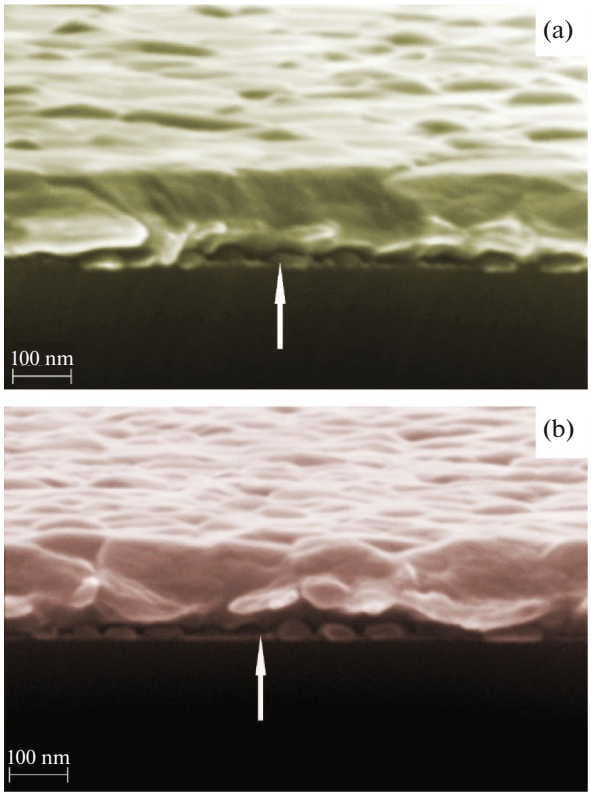

Fig. 6. SEM image of fractures of samples of magnetron films of aluminum on silicon depending on the ratio k = O (at %)/Al(at %) according to quantitative X-ray microanalysis (EDS): k = (a) 0.14 (TA5) and (b) 0.26 (HBL) [29]. Arrows indicate the inner film-substrate boundary.

ple TA5 among those studied in this study (Table 1). The AFM data show that the surface morphology of the films studied in this study has differences, but they are not significant and cannot be an explanation for the observed R_{02} dependencies of specific resistance in Fig. 1. At the same time, the AFM images of 60 nm MBE films [31] clearly show that they have a large intergranular space: they are loose. It should be noted that the surface morphology is adequately described by the correlation length and the Hurst parameter, provided that a series of films are formed under the same technological conditions. However, a slight difference in the conditions of preparation of the growth chamber leads to a change in the surface morphology and parameters of the films (cf. HBF [29] and TA5 (Table 1)). As a result, the transport properties of the films change. This fact must be taken into account when comparing the absolute values of the morphological parameters of the surface images of films grown even under slightly different growth conditions.

The density profiles of the studied aluminum films with homobuffered HBL layers deposited at temperatures of 300, 600, and 700 K are presented in Fig. 5. The table also shows horizontal dashed lines (bulk Si, bulk Al) showing the density values for bulk silicon (2.33 g/cm^3) and aluminum (2.699 g/cm^3) [34], respectively. It can be seen that despite the general expected trend of the dependence of the density of thin magnetron films on thickness, the density profiles differ qualitatively and quantitatively.

The profile view in Fig. 5 shows that the density of the aluminum film with the HBL 700 K layer has a constant value of D = 2.66 g/cm^3 over a thickness of 30–130 nm. The film density at the boundary with the substrate and near the surface, in the first approximation, changes linearly, forming transition layers of 30 and 25 nm, respectively. It should be noted that these values are averaged over an area of 100 mm^2 of the heights of the hills visible in Fig. 6 on the surface of the film and are not adequate for comparison with the rms value (Table 1).

Roughnesses of 5–6 nm should have completely extinguished the specular reflection of X-ray radiation and made it impossible to conduct XRR studies. The thickness of the film-substrate transition layer is comparable to the height of the crystallites in the HBL [38]. In contrast, the film density of the TA1 sample with an HBL 300 K layer has a quasi-linear dependence with increasing film thickness and barely reaches 2.5 g/cm^3 at a thickness of 80 nm. This result is not surprising and is expected for island films up to a thickness of $t \leq$ 120 nm. It should be noted that the size of crystallites in the HBL before the subsequent deposition of aluminum, formed at room temperature (300 K), is 20 nm [38]. Films with the HBL, which was deposited at other temperatures (Table 1), turned out to be less dense in thickness. For comparison, Fig. 5 shows the density distribution for the Al film of sample TA4 with a 600 K HBL layer. This film has a fairly uniform thickness profile with a density of D = 2.60 g/cm^3. A lower density value compared to the density of the film with the HBL 700 K layer necessarily leads to a lower amplitude of oscillations (without taking into account their attenuation due to the roughness at the film boundaries [28]) on the XRR curves (Fig. 3) of the samples. In addition, the density gradient in the substrate-film transition layer is smaller, which is associated with its lower average density due to voids and amorphous phases. Therefore, we can confidently say that the TA4 film will have a higher residual resistance. Finally, the results of our studies obtained by the XRR method provide a density key for an a priori explanation of the difference in the specific resistances of MBE films of 60 nm [31] and 60 nm [32] observed in Fig. 1.

Electron microscopic images of chips of two-stage Al films on Si(111), sputtered depending on the heating time and pumping of the magnetron chamber, are shown in Figs. 6a and 6b. The chips clearly show that the thickness of the transition layer of the TA5 film (a) is approximately half that of the thickness of the layer for the HBL film [29] (b) with fast pumping. The observed changes in the thickness of the HBL, microstructure, and surface morphology of the film (b) are

associated with a higher value of residual oxygen impurity in the sputtering chamber of the magnetron. As a result, changes in the specified characteristics of the film will lead to a decrease in its density and an increase in specific resistance.

CONCLUSIONS

This paper presents the results of studies of the relationship between the temperature dependence of the specific resistance and the structural features of 150-nm Al films on an Si(111) substrate. The films were deposited by magnetron sputtering in a two-stage growth mode with the formation of an HBL on the substrate surface at temperatures of 300–800 K. The real structure of the films was studied by a combination of complementary methods: AFM, SEM, EDS, XRD, GIXRD, and XRR. It is shown that despite the sensitivity of local microscopic methods, they provide a controversial picture of the internal structure of films, which cannot be unambiguously linked to the laws of specific resistance. X-ray diffraction in a symmetrical scheme and at grazing angles of incidence made it possible to reliably record only the quantitative difference in the texture of the films, and not in the sizes of their crystallites. Thus, no answer was obtained about a clear relationship with the specific resistance of the film. The most unambiguous data (density distribution profile) for characterizing films and establishing a relationship with their resistance were obtained by X-ray reflectometry.

Based on the approach proposed in this study for analyzing the specular reflection of X-rays, we have shown that magnetron films of aluminum with a 700 K HBL reach the density of the bulk material at a thickness of 40 nm. The temperature dependence of its resistance is analogous to ρ_b of the sample of bulk material in the range from 300 to 150 K. In the range of helium temperatures, the film with a 700-K HBL has minimal residual resistance compared to films deposited on HBLs of other temperatures. The main contribution to the resistance will be given by scattering at the boundaries of small grains, as well as distortions of the internal boundary and surface roughness. In contrast, the Al film with a 300-K HBL reaches the density of the bulk material only at a thickness of 120 nm and is less dense or loose due to the voids between the grains–crystallites. The resistance of such a film is significantly higher than ρ_b at 300 K and depends weakly on temperature due to the large number of cavities in its volume, whose composition and boundaries create the main contribution to the resistance during the directed movement of electrons.

Thus, the conducted studies have shown that X-ray specular reflection (XRR) can significantly help in developing growth conditions for other metal films, their certification, and predicting the temperature dependence of their resistance.

FUNDING

The work by A.A. Lomov and A.A. Tatarintsev was carried out as part of a state assignment of the National Research Center "Kurchatov Institute." The work by M.A. Tarasov and A.M. Chekushkin was carried out with the financial support of the Russian Science Foundation, project no. 23-79-00022 "Structural and electrophysical characteristics of superconducting aluminum films and tunnel junctions based on them."

CONFLICT OF INTEREST

The authors of this work declare that they have no conflicts of interest.

REFERENCES

1. Wang, H. and Blaabjerg, F., Reliability of capacitors for DC-link applications in power electronic converters—An overview, *IEEE Trans. Ind. Appl.*, 2014, vol. 50, no. 5, pp. 3569–3578. https://doi.org/10.1109/tia.2014.2308357
2. Drozdov, M.N., Drozdov, Y.N., Chkhalo, N.I., Polkovnikov, V.N., Yunin, P.A., Chirkin, M.V., Gololobov, G.P., Suvorov, D.V., Fu, D.J., Pelenovich, V., and Tolstogouzov, A., Time-of-flight secondary ion mass spectrometry study on Be/Al-based multilayer interferential structures, *Thin Solid Films*, 2018, vol. 661, pp. 65–70. https://doi.org/10.1016/j.tsf.2018.07.013
3. Dubey, A., Mishra, R., Hsieh, Yu., Cheng, Ch., Wu, B., Chen, L., Gwo, Sh., and Yen, T., Aluminum plasmonics enriched ultraviolet GaN photodetector with ultrahigh responsivity, detectivity, and broad bandwidth, *Adv. Sci.*, 2020, vol. 7, no. 24, p. 2002274. https://doi.org/10.1002/advs.202002274
4. Earnest, C.T., Béjanin, J.H., McConkey, T.G., Peters, E.A., Korinek, A., Yuan, H., and Mariantoni, M., Substrate surface engineering for high-quality silicon/aluminum superconducting resonators, *Supercond. Sci. Technol.*, 2018, vol. 31, no. 12, p. 125013. https://doi.org/10.1088/1361-6668/aae548
5. Clarke, J. and Braginski, A.I., *The SQUID Handbook*, vol. 1: *Fundamentals and Technology of SQUIDS and SQUID Systems*, Cambridge: Wiley-VCH, 2002.
6. Mantegazzini, F., Ahrens, F., Borghesi, M., Falferi, P., Fasolo, L., Faverzani, M., Ferri, E., Labranca, D., Margesin, B., Mezzena, R., Moretti, R., Nucciotti, A., Origo, L., Vinante, A., Zannoni, M., and Giachero, A., High kinetic inductance NbTiN films for quantum limited travelling wave parametric amplifiers, *Phys. Scr.*, 2023, vol. 98, no. 12, p. 125921. https://doi.org/10.1088/1402-4896/ad070d
7. Khukhareva, I.S., The superconducting properties of thin aluminum films, *Sov. Phys. JETP*, 1963, vol. 16, no. 4, pp. 828–832.
8. Tarasov, M., Gunbina, A., Fominsky, M., Chekushkin, A., Vdovin, V., Koshelets, V., Sohina, E., Kalaboukhov, A., and Edelman, V., Fabrication of NIS and SIS nanojunctions with aluminum electrodes and studies of magnetic field influence on IV curves, *Electronics*,

2021, vol. 10, no. 23, p. 2894.
https://doi.org/10.3390/electronics10232894

9. Yeh, C.-C., Do, T.-H., Liao, P.-C., Hsu, C.-H., Tu, Y.-H., Lin, H., Chang, T.-R., Wang, S.-C., Gao, Y.-Y., Wu, Y.-H., Wu, C.-C., Lai, Yu.A., Martin, I., Lin, S.-D., Panagopoulos, Ch., and Liang, C.-T., Doubling the superconducting transition temperature of ultraclean wafer-scale aluminum nanofilms, *Phys. Rev. Mater.*, 2023, vol. 7, no. 11, p. 114801. https://doi.org/10.1103/physrevmaterials.7.114801
10. Lee, Yo.J. and Kang, S.-W., Study on the characteristics of alumdinum thin films prepared by atomic layer deposition, *J. Vac. Sci. Technol., A*, 2002, vol. 20, no. 6, pp. 1983–1988. https://doi.org/10.1116/1.1513636
11. Buckel, W. and Kleiner, R., *Superconductivity: Fundamentals and Applications*, Weinheim: Wiley, 2008.
12. Wu, W., Brongersma, S.H., Van Hove, M., and Maex, K., Influence of surface and grain-boundary scattering on the resistivity of copper in reduced dimensions, *Appl. Phys. Lett.*, 2004, vol. 84, no. 15, pp. 2838–2840. https://doi.org/10.1063/1.1703844
13. Munoz, R.C. and Arenas, C., Size effects and charge transport in metals: Quantum theory of the resistivity of nanometric metallic structures arising from electron scattering by grain boundaries and by rough surfaces, *Appl. Phys. Rev.*, 2017, vol. 4, no. 1, p. 11102. https://doi.org/10.1063/1.4974032
14. Thomson, J.J., On the theory of electric conduction through thin metallic films, *Proc. Camb. Philos. Soc.*, 1901, vol. 11, p. 120.
15. Kamerlingh-Onnes, H., Contributions to the knowledge of the ψ surface of van der Waals. XI. A gas that sinks in a liquid, *Proc. K. Akad.*, 1906, vol. 9, p. 459.
16. Fuchs, K., The conductivity of thin metallic films according to the electron theory of metals, *Math. Proc. Cambridge Philos. Soc.*, 1938, vol. 34, no. 1, pp. 100–108. https://doi.org/10.1017/s0305004100019952
17. Sondheimer, E.H., The mean free path of electrons in metals, *Adv. Phys.*, 2001, vol. 50, no. 6, pp. 499–537. https://doi.org/10.1080/00018730110102187
18. Mayadas, A.F., Shatzkes, M., and Janak, J.F., Electrical resistivity model for polycrystalline films: The case of specular reflection at external surfaces, *Appl. Phys. Lett.*, 1969, vol. 14, no. 11, pp. 345–347. https://doi.org/10.1063/1.1652680
19. Mayadas, A.F. and Shatzkes, M., Electrical-resistivity model for polycrystalline films: The case of arbitrary reflection at external surfaces, *Phys. Rev. B*, 1970, vol. 1, no. 4, pp. 1382–1389. https://doi.org/10.1103/physrevb.1.1382
20. Pyataikin, I.I., Influence of the grain size effect on the coefficients of reflection, transmission, and absorption of microwaves by the polycrystalline metal films, *Zhurnal Radioelektroniki*, 2020, vol. 2020, no. 10, pp. 1–29. https://doi.org/10.30898/1684-1719.2020.10.5
21. Zhang, W., Brongersma, S.H., Richard, O., Brijs, B., Palmans, R., Froyen, L., and Maex, K., Influence of the electron mean free path on the resistivity of thin metal films, *Microelectron. Eng.*, 2004, vol. 76, nos. 1–4, pp. 146–152. https://doi.org/10.1016/j.mee.2004.07.041
22. Bakonyi, I., Accounting for the resistivity contribution of grain boundaries in metals: critical analysis of reported experimental and theoretical data for Ni and Cu, *Eur. Phys. J. Plus*, 2021, vol. 136, no. 4, p. 410. https://doi.org/10.1140/epjp/s13360-021-01303-4
23. Chubov, P.N., Eremenko, V.V., and Pilipenko, Y.A., Dependence of the critical temperature and energy gap on the thickness of superconducting aluminum films, *Sov. Phys. JETP*, 1969, vol. 28, no. 3, pp. 389–395.
24. Pettit, R.B. and Silcox, J., Film structure and enhanced superconductivity in evaporated aluminum films, *Phys. Rev. B*, 1976, vol. 13, no. 7, pp. 2865–2872. https://doi.org/10.1103/physrevb.13.2865
25. Amirov, I.I., Selyukov, R.V., Naumov, V.V., and Gorlachev, E.S., Influence of deposition conditions and ion-plasma treatment of thin cobalt films on their electrical resistivity, *Russ. Microelectron.*, 2021, vol. 50, no. 1, pp. 1–7. https://doi.org/10.1134/s1063739721010030
26. Parratt, L.G., Surface studies of solids by total reflection of X-rays, *Phys. Rev.*, 1954, vol. 95, no. 2, pp. 359–369. https://doi.org/10.1103/PhysRev.95.359
27. Kiessig, H., Interferenz von Röntgenstrahlen an dünnen Schichten, *Ann. Phys.* (Berlin, Ger.), 1931, vol. 402, no. 7, pp. 769–788. https://doi.org/10.1002/andp.19314020702
28. Holý, V., Pietsch, U., and Baumbach, T., *High-Resolution X-Ray Scattering from Thin Films and Multilayers*, Springer Tracts in Modern Physics, vol. 149, Berlin: Springer, 1999. https://doi.org/10.1007/BFb0109385
29. Lomov, A.A., Zakharov, D.M., Tarasov, M.A., Chekushkin, A.M., Tatarintsev, A.A., Kiselev, D.A., Ilyina, T.S., and Seleznev, A.E., Influence of the homobuffer layer on the morphology, microstructure, and hardness of Al/Si (111) films, *Tech. Phys.*, 2024, vol. 69, no. 6, pp. 1636–1645. https://doi.org/10.1134/S1063784224060239
30. Wormington, M., Panaccione, Ch., Matney, K.M., and Bowen, D.K., Characterization of structures from X-ray scattering data using genetic algorithms, *Philosophical Transactions of the Royal Society of London. Series A: Mathematical, Physical and Engineering Sciences*, 1999, vol. 357, no. 1761, pp. 2827–2848. https://doi.org/10.1098/rsta.1999.0469
31. Aswal, D.K., Joshi, N., Debnath, A.K., Gupta, S.K., Vuillaume, D., and Yakhmi, J.V., Thickness dependent morphology and resistivity of ultra-thin Al films grown on Si(111) by molecular beam epitaxy, *Phys. Status Solidi A*, 2006, vol. 203, no. 6, pp. 1254–1258. https://doi.org/10.1002/pssa.200566102
32. Sedov, E.A., Investigation of the critical temperature of superconducting transition of aluminum thin films, *Cand. Sci. (Eng.) Dissertation*, Moscow: HSE University, 2024.
33. Desai, P.D., James, H.M., and Ho, C.Y., Electrical resistivity of aluminum and manganese, *J. Phys. Chem. Ref. Data*, 1984, vol. 13, no. 4, pp. 1131–1172. https://doi.org/10.1063/1.555725
34. Samsonov, G.V., *Handbook of the Physicochemical Properties of the Elements*, Springer, 1968. https://doi.org/10.1007/978-1-4684-6066-7

35. Nečas, D. and Klapetek, P., Gwyddion: An open-source software for SPM data analysis, *Open Phys.*, 2012, vol. 10, no. 1, pp. 181–188. https://doi.org/10.2478/s11534-011-0096-2

36. Horcas, I., Fernández, R., Gómez-Rodríguez, J.M., Colchero, J.W.S.X., Gómez-Herrero, J.W.S.X.M., and Baro, A.M., WSXM: A software for scanning probe microscopy and a tool for nanotechnology, *Rev. Sci. Instrum.*, 2007, vol. 78, no. 1, p. 13705. https://doi.org/10.1063/1.2432410

37. Shvartsman, V.V. and Kholkin, A.L., Evolution of nanodomains in $0.9PbMg_{1/3}Nb_{2/3}O_3$-$0.1PbTiO_3$ single crystals, *J. Appl. Phys.*, 2007, vol. 101, no. 6, p. 64108. https://doi.org/10.1063/1.2713084

38. Lomov, A.A., Zakharov, D.M., Tarasov, M.A., Chekushkin, A.M., Tatarintsev, A.A., and Vasiliev, A.L., Al islands on Si(111): Growth temperature, morphology, and strain, *Russ. Microelectron.*, 2024, vol. 53, no. 4, pp. 339–348. https://doi.org/10.1134/s1063739724600468

39. Croce, P. and Névot, L., Étude des couches minces et des surfaces par réflexion rasante, spéculaire ou diffuse, de rayons X, *Rev. Phys. Appl.*, 1976, vol. 11, no. 1, pp. 113–125. https://doi.org/10.1051/rphysap:01976001101011300

40. Artioukov, I.A., Asadchikov, V.E., and Kozhevnikov, I.V., Effects of a near-surface transition layer on X-ray reflection and scattering, *J. X-Ray Sci. Technol.*, 1996, vol. 6, no. 3, pp. 223–243. https://doi.org/10.3233/xst-1996-6301

41. Afanas'ev, A.M., Chuev, M.A., Imamov, R.M., Lomov, A.A., Mokerov, V.G., Fedorov, Y.V., and Guk, A.V., Study of multilayer GaAs-$In_xGa_{1-x}As$ layer-based structure by double-crystal X-ray diffractometry, *Crystallogr. Rep.*, 1997, vol. 42, no. 3, pp. 467–476.

42. Press, W.H. et al., *Numerical Recipes in C*, New York: Cambridge University Press, 1996.

43. Dobierzewska-Mozrzymas, E. and Warkusz, F., Size effects in epitaxial aluminium films, *Thin Solid Films*, 1977, vol. 43, no. 3, pp. 267–273. https://doi.org/10.1016/0040-6090(77)90288-7

44. Ashcroft, N.W. and Mermin, N.D., *Solid State Physics*, Philadephia: WB Saunders, 1976.

45. Birkholz, M., *Thin Film Analysis by X-Ray Scattering*, Wiley, 2006. https://doi.org/10.1002/3527607595